Design and Analysis of Embedded I&C for A Fully Submerged Magnetically Suspended Impeller Pump *

Alexander M. Melin[a,*] and Roger A. Kisner[a]

[a] *Oak Ridge National Laboratory, Sensors and Embedded Systems Group*
1 Bethel Valley Road, Oak Ridge, TN 37831

*Email: melina@ornl.gov

Number of pages: 24

Number of tables: 2

Number of figures: 10

Abstract

Improving nuclear reactor power system designs and fuel processing technologies for safer and more efficient operation require the development of new component designs. In particular, many of the advanced reactor designs such as the molten salt reactors and high-temperature gas cooled reactors have operating environments beyond the capability of most currently available commercially components. To address this gap, new cross-cutting technologies need to be developed that will enable design, fabrication, and reliable operation of new classes of reactor components. The Advanced Sensor Initiative (ASI) of the Nuclear Energy Enabling Technologies (NEET) initiative is investigating advanced sensor and control designs that are capable of operating in these extreme environments. Under this initiative, Oak Ridge National Laboratory (ORNL) has been developing embedded instrumentation and control for extreme environments. To develop, test, and validate these new sensing and control techniques, ORNL is building a pump testbed that utilizes submerged magnetic bearings to levitate the shaft. The eventual goal is to apply these techniques to a high-temperature (700 °C) canned rotor pump that utilizes active magnetic bearings to eliminate the need for mechanical bearings and seals. The technologies will benefit the Next Generation Power Plant, Advanced Reactor Concepts, and Small Modular Reactor programs. In this paper, we will detail the design and analysis of the embedded I&C testbed with submerged magnetic bearings focusing on the interplay between the different major systems. Then we will analyze the forces on the shaft and their role in the magnetic bearing design. Next, we will develop the radial and thrust bearing geometries needed to meet the operational requirements of the testbed. Finally, we will present some initial system identification results to validate the theoretical models of the testbed dynamics.

Keywords — Embedded I&C, Active Magnetic Bearings, Advanced Control, Extreme Environments, High-Temperature Pumps, Submerged Pumps, Molten Salt Reactor

I. INTRODUCTION

Improving nuclear reactor safety, efficiency, and cost are necessary to nuclear power's continued use as an important electricity generation source. Often times, these improvements require that reactor systems operate in extreme environments not seen in current designs. These extreme environments can include high temperatures, high pressures, corrosive materials, and high radiation. In these new extreme operating environments, many current component designs will not provide sufficient safety, performance, and reliability. In fact, many existing component technologies will not function at all in these operational environments. Embedded instrumentation and control (I&C) is one technology that will enable new component designs for extreme environments. However, new cross-cutting technologies need to be developed for instrumentation and control for extreme environments to meet design, safety, and performance goals.

The Advanced Sensors Initiative (ASI), a program of the Department of Energy's Nuclear Energy Enable Technologies (NEET) initiative is funding research into new cross-cutting technologies to enable new classes of reactor components to overcome the challenges of operating in extreme environments. In particular, the ASI program focuses on new sensor and control techniques including embedded instrumentation and control. Under this program, Oak Ridge National Laboratory (ORNL) is researching high-temperature (700 °C) magnetic bearings for use in reactor components such as fluid pumps and turbines. Developing high-temperature magnetic bearings requires the development of high-temperature electromagnetics which will enable new component, sensor, and actuator designs.

The initial phase of the project developed a conceptual high-temperature reactor coolant pump utilizing magnetic bearings. This component was chosen due to the design challenges posed by the extreme operating environment and the potential for improved performance, safety, and reliability from embedded I&C.[1, 2, 3] This project phase identified pump configurations, functional materials, sensors, and control techniques that would be suitable for high-temperature operation. After study, a canned rotor pump (i.e. the internal components of the pump are in direct contact with the pumped fluid and protected by a barrier material) was chosen as the configuration for the conceptual pump. The use of active magnetic bearings in the pump design removes the need for mechanical bearings and seals that are the main cause of maintenance costs and failures.[4, 5, 6, 7] The design feasibility and manufacturability of the conceptual pump design were studied.[8] This

early phase of the project also developed detailed models of the coupled electromagnetics and rotordynamics including the nonlinear hydrodynamic forces in the fluid gap between the rotor and stator due to the canned pump design[9].

The next phase of the project was creation of a laboratory scale magnetic bearing testbed. This testbed was used to investigate closed-loop system identification techniques, develop stabilizing controllers, validate theoretical models, and create software toolsets for the design and analysis of magnetic bearing geometries and controls.[10]

The third project phase currently underway is the development of a unique submerged magnetic bearing testbed where the bearings are in contact with the fluid [11]. This low-temperature testbed emulates the dynamics of the high-temperature canned rotor pump. As far as the authors are aware, this will be the first magnetic bearing to operate submerged in fluid. The SKF company has built an undersea gas compression system that uses magnetic bearings, but the bearings are not in contact with the surrounding seawater. The ORNL submerged magnetic bearing testbed will be a fully operational water pump with a shaft that is levitated using two radial and two omnidirectional thrust magnetic bearings. This testbed will be used to develop the foundational technologies needed for high-temperature operation. This development effort includes modeling, closed-loop system identification, sensorless magnetic bearing operation, and advanced control design strategy in conjunction with material, mechanical, electro-magnetic, and electro-mechanical design.

Magnetic bearings have been in use for decades and are well suited to challenging environments. They have seen widespread use in cryogenic pumps and expanders, turbopumps, steam turbines, hot helium blowers, flywheel energy storage, and high-speed transportation, levitating trains, and high-speed machinery [12, 13, 14]. They are also commonly used in aerospace gyroscopes, momentum wheels, and vacuum turbopumps. Currently magnetic bearings operate in air or vacuum and the external forces on the shaft are not considered because they are small or treated as a bounded external force when designing the magnetic bearing controller. However, in a canned pump design like the ORNL high-temperature conceptual pump, the shaft will experience nonlinear hydrodynamic forces that can exhibit complex behavior such as speed dependent Taylor-Couette flow bifurcation.[15] Existing models and control design techniques for magnetic bearings are not sufficient for systems with these nonlinear hydrodynamics.

The ORNL testbed will emulate the nonlinear hydrodynamics of the high-temperature conceptual pump designed by ORNL.[1] The goal of the testbed is to provide a realistic platform to developing, validating, and testing new models and embedded instrumentation and control systems that can stabilize the magnetic bearings in the presence of the nonlinear fluid forces.

Most magnetic bearing research focuses on new geometric configurations and control theory. The most common magnetic bearing control design method is to linearize the system about the operating point and create independent proportional-integral-derivative (PID) controllers for each axis.[14, 13] This decoupled control design assumes that the shaft is rigid and well balanced and that gyroscopic and other external shaft forces are minimal. For many operational environments these assumptions are valid. For example, vacuum turbopumps have minimal aerodynamic forces on the shaft and very precisely balanced shafts because they operate at high rotational speeds. Much of the research into control design for magnetic bearings has focused on relaxing these assumptions. In [16] and [17] fuzzy-logic based controllers for magnetic bearings are developed. Other nonlinear controllers developed for magnetic bearings use sliding-mode control [18, 19]. Robust controllers are typically used in magnetic bearings to compensate for vibrations due to shaft imbalances and flexible mode shapes. In [20] a robust controller is developed based on eigenstructure assignment. An H_∞ robust controller for shaft imbalance compensation was developed in [21]. An adaptive controller was developed in [22] to perform shaft auto-centering with an unknown mass imbalance on the rotor.

There has also been interest in the development of *sensorless bearings* or *self-sensing* magnetic bearings. These bearing designs do not explicitly use shaft position sensors. Self-sensing bearing techniques are the only viable option for magnetic bearing control above 450 $^\circ$ C until high-temperature position sensors are available. Self-sensing techniques are still being researched and the difficulty in practical implementation means that currently there are no commercially available self-sensing magnetic bearings. There are two main techniques for self-sensing bearings [13]. The first technique uses the existing pulse-width modulated signal from the power electronics to create a current ripple in the coil windings. The amplitude of this ripple is proportional to the shaft position. The second main technique for self-sensing is the family of Kalman filters. Theoretically, the shaft position is observable using only the magnetic bearing coil currents because of the coupling between the shaft motion and the bearing electromagnetic dynamics. In practice Kalman

techniques suffer from poor performance due to uncertainties, a lack of persistent excitation, and nonlinearities in the system. In [23], the robustness limitation of self-sensing magnetic bearings is investigated and compared to bearing control using shaft position sensors. In [24] a wavelet based shaft position estimator is developed. A self-sensing three-pole magnetic bearing using the Kalman filter was developed in [25] and extended to use the Unscented Kalman Filter in [26].

The remaining sections of the paper will provide details about the ORNL submerged magnetic bearing testbed design. In section II, the design concept for the testbed is discussed. In section III the worst-case impeller forces that constrain the magnetic bearing geometry are described. In section IV, the geometry and force dynamics of the radial bearing design are discussed. In section V, the design of the axial bearing is discussed including optimizing the geometry and force characteristics of the bearing. In section VI, the impact of the magnetic bearing geometry on the coil dynamics and control stability is discussed and some experimental results of system identification tests are presented. Section VII concludes the paper and future work is discussed.

II. DESIGN CONCEPT

To reduce the cost and time needed for design and fabrication of an induction motor driven pump, a commercial canned rotor pump was chosen to be the foundation of the testbed. Canned rotor pumps operate with the rotor and stator submerged in the pumped fluid and utilize a thin metal 'can' around the electromagnetic components to prevent their contact with the fluid. The pump selected was a Teikoku 204TF1 impeller pump. The nominal pump flow rate at 3450 RPM is 511 L/min with a nominal head of 75 m. To create the testbed, the original pump is retrofitted with active magnetic bearings that replace its existing graphite fluid bearings. This retrofit requires extensive modification to the original pump but allows the use of the existing 3600 RPM induction motor, impeller, and volute. The pump was disassembled then each component was measured and modeling in 3D because detailed manufacturing drawings of the Teikoku pump were not available. The solid model of the unmodified pump is shown in figure 1 without the volute. After the development of an accurate solid model of the original pump, the design was modified to add two radial and two omni-directional thrust magnetic bearings at each end of the shaft. To make room for the magnetic bearings shaft extensions are used on either end of the existing shaft. The shaft extensions mount the radial magnetic bearing laminations and the thrust bearing rotors. The

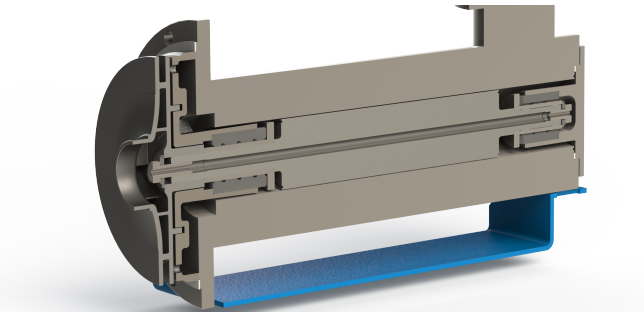

Fig. 1. 3D Model of the Teikoku 204TF1 pump created after disassembly and measurement.

radial magnetic bearing laminations are made of M19 electrical steel and the thrust bearing is made from grade 410 martensitic stainless steel.

Figure 2 shows the final design of the modified Teikoku 204TF1 pump and figure 3 shows a closer view of the front magnetic bearing.

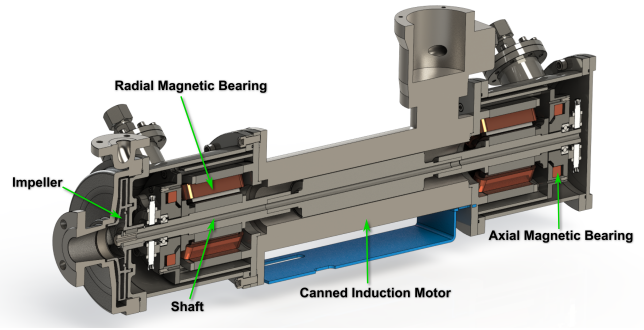

Fig. 2. 3D Model of the modified Teikoku 204TF1 pump magnetic bearing testbed.

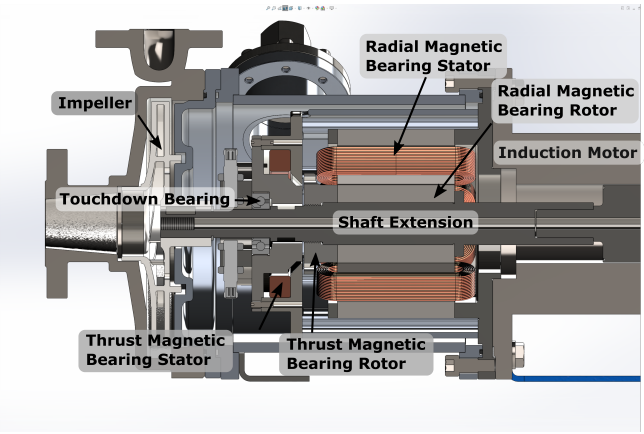

Fig. 3. Closer view of the combined front thrust and radial magnetic bearings.

The radial bearing design is a magnetic reluctance force based bipolar design that eliminates the need for permanent magnets. Geometry and assembly constraints limit the diameter of the thrust bearing rotor; therefore, to minimize the size of the thrust bearing stator an offset flux path is used. This configuration allows the magnetic coils to be offset from the rotor stator airgap. The thrust bearing is split into front and rear omni-directional bearings. This configuration which minimizes nonlinear magnetic field interactions in the thrust bearing stator also increases the maximum available magnetic field strength before saturation. Two touchdown bearings are mounted into the thrust bearings to prevent the rotor from touching the stator when the magnetic bearings are not operating or in the event of a failure.

When designing magnetic bearings, it is important to consider the entire system because of the close coupling between the mechanical, electromagnetic, and control systems. The three critical design parameters are the shaft forces due to the impeller, the maximum rotational speed, and the dynamics of the magnetic coil. The maximum impeller forces provide a lower bound for the magnetic flux path geometry. The maximum rotational speed of the shaft provides a lower bound on the bandwidth of magnetic coil current response. The rotational speed also impacts the impeller forces. Finally, the geometry influences the linearized dynamics of the shaft, which in turn provides another bound on the control system bandwidth.

III. IMPELLER FORCES

The magnetic bearing force is proportional to the cross sectional area of the magnetic flux path as seen in equations (4) and (5). The active magnetic bearings must have sufficient force capacity to overcome any shaft forces over the full range of the shaft movement ($\pm$ 0.75 mm). The primary forces on the shaft are due to gravity, fluid forces on the impeller, and position dependent hydrodynamic forces on the shaft. Typically magnetic bearings operate in air or vacuum and the position dependent hydrodynamic forces on the shaft are ignored. In this design, the hydrodynamic forces due to the small fluid filled gap between the rotor and stator cannot be ignored. In [9], the authors present a method for calculating these forces. Since the hydrodynamic forces act to restore the shaft to a centered position and they reduce to a torque when the shaft is centered during operation, we will only consider the impeller forces in the design of the bearing geometry.

The impeller/volute geometry and the operating condition of the pump defines the fluid

forces acting on the impeller. The Teikoku 204TF1 impeller has a single volute design, closed impellers, balance holes, and a back ring.

The radial loading of the pump is affected by the volute design and the fraction of operating capacity (how far from the best efficiency point (BEP)) the pump is operating at. The radial load is given by

$$F_r = \frac{K_r H D B S_G}{1.02 \times 10^{-4}} \tag{1}$$

where K_r is a radial thrust factor, H is the impeller head at the flow point in m, D is the impeller diameter in m, and B is the impeller width at the vane discharge including the shroud in m and S_G is the specific gravity of the fluid being pumped [27]. Table I summarizes the relevant physical parameters and radial forces on the Teikoku 204TF1 pump with the minimum and maximum expected values in parenthesis.

TABLE I
Teikoku 204TF1 Radial Forces

Parameter	Value	Units
K_r	(0.09, 0.38)	
H	(54.9, 88.4)	m
D	0.208	m
B	0.0158	m
S_G	1.0	
F_r	(159.2, 1082.3)	N

The axial loading of the pump is affected by the pump flow rate and the pressure differential created between the front and rear of the impeller and the impeller design [27]. Calculations for axial impeller forces are highly uncertain. Fortunately, Teikoku tests all of their pump designs to determine the actual axial impeller forces. For the 204TF1 pump, their expected maximum axial force is 600 N and their tests show that the maximum measured axial force for the 0.208 m (8.188 in) diameter impeller is 510 N (52 kgf).

IV. RADIAL BEARING

The forces on both radial bearings due to fluid forces on the impeller can be calculated based on the distances from the impeller to the bearings. We will denote the impeller as the 'front' of the pump, the $Z+$ direction from the center of mass towards the impeller, and the radial bearing

that is the closest to the impeller as the front bearing or bearing A. The bearing furthest from the impeller will be denoted as the rear bearing or bearing B. The distance from bearing A to the impeller outlet denoted by L_A is approximately 0.27 m and the distance from bearing B to the impeller outlet denoted by L_B is approximately 0.860 m.

Using the following simple moment balance equations, the worst case reaction forces at the bearings F_A and F_B can be calculated.

$$F_A = F_r - F_B \tag{2}$$

$$F_B = F_r \frac{L_A}{L_B} \tag{3}$$

Given a maximum radial force of $F_r = 1082\ N$, bearing A needs to create at least 742 N of force and bearing B will need to create at least 339 N. To account for any uncertainties in the forces on the shaft, both radial magnetic bearings are designed to create a maximum force of 2000 N.

The radial magnetic bearings will use a differential bearing driving mode. This mode utilizes a bias current i_0 to linearize the relationship between the bearing force and the control current $u_i(t)$ for $u_i(t) \in [-i_0, i_0]$. The nonlinear force created by the radial magnetic bearing for a bipolar mode magnetic bearing can be calculated for a rotor position x and control current u_i by [14, 13]

$$F = k \left(\frac{(i_0 + u_i)^2}{(x_0 - x)^2} - \frac{(i_0 - u_i)^2}{(x_0 + x)^2} \right) \cos \alpha \tag{4}$$

with

$$k = \frac{1}{4} \mu_0 N^2 A \tag{5}$$

where N is the number of turns in the magnetic bearing coil, x_0 is the nominal airgap between the stator and rotor, and A is the minimum cross sectional area of the magnetic flux path. Assuming that the bearing operates in a region about $x = 0$ we can linearize (4) about the operating points $x = 0$ and $u_i = 0$ yielding the expression of the bearing force given by[14, 13]

$$F_l = k_i u_i + k_x x \tag{6}$$

where

$$k_i = \frac{4ki_0}{x_0^2} \tag{7}$$

$$k_x = \frac{4ki_0^2}{x_0^3} \tag{8}$$

Equations (5), (7), and (8) show that the linearized force characteristics of the bearing are only due to the number of turns in the coil N, the cross sectional area of the magnetic flux A, the nominal airgap x_0, and the linearizing bias current i_0. Consequently, these are the primary design parameters for magnetic bearings.

Another important consideration in designing the bearing geometry is magnetic saturation. The magnetic bearing force can also be expressed as

$$F = \frac{B^2 A}{\mu_0} \tag{9}$$

where B is the magnetic field strength and μ_0 is the magnetic permeability of vacuum. Using 9 we can calculate the minimum magnetic flux cross sectional area for the bearing stator. The stator is made from M19 electricl steel so, using the maximum desired radial force of 2000 N and a maximum magnetic field strength of 1.4 T which is the upper bound on the linear region of the M19 electrical steel B-H curve, the minimum cross sectional area needed for the radial bearings is 1283 mm^2. The total number of turns N in the magnetic bearing coil is related to the maximum magnetic field strength of 1.4 T and the maximum steady state current supplied by the power electronics. Using a maximum current of $u_i = 20$ A the desired number of turns in the magnetic bearing coil is calculated to be $N = 167$ using

$$N = \frac{2Bx_0}{\mu_0 u_i} \tag{10}$$

The bearing coil windings will use 16 AWG wire, which has a nominal steady state current limit of 20 A. Now the radial stator geometry can be set. The stator tooth width, inner and outer radius, and stack length are optimized to balance the magnetic cross sectional area, coil cross sectional area, and stator mass.

Based on these design constraints the final geometry and coil parameters are shown in Table

II.

TABLE II
Radial Bearing Geometry

Parameter	Value	Units	Description
x_0	0.0015	m	Air Gap
i_0	8.0	A	Bias Current
d_r	0.066	m	Rotor OD
h_t	0.030	m	Tooth Height
w_t	0.0129	m	Tooth Width
h_s	0.100	m	Stack Height
N	167	$turns$	Total Coil Turns
α	22.5°	deg	Tooth Angle

The geometry chosen defines the linearized dynamics of the shaft. For this radial bearing design, $k_i = 136.3$ and $k_x = 727044.6$. The linearized force position term can be thought of as a destabilizing virtual spring attached to the shaft. This virtual spring can be related to a shaft fundamental frequency using the equation

$$\omega = \sqrt{\frac{k_x}{m}} \tag{11}$$

where m is the mass of the shaft. For the final design with a shaft mass of 18.3391 kg the fundamental shaft frequency is 199 rad/s (31.6 Hz).

Figure 4 shows both the theoretical linearized force characteristics of the radial bearing differential drive design which is validated by calculating the nonlinear magnetic forces using experimentally measured material properties for M19 electrical steel.

The radial bearing geometry was designed at the nominal operating point of the system. However, during startup, the shaft starts resting on the touchdown bearings which means that there is a significantly larger airgap in the vertical direction that reduces the maximum force available to lift the shaft to its operating position; therefore we need to ensure that the bearing will have sufficient force at the limits of the radial motion to overcome weight of the shaft. Calculations show that during startup, the magnetic bearing needs to produce at least 180 N of force on the shaft in the vertical direction. Figure 5 verifies the nonlinear force produced by the radial bearing when it is resting on the touchdown bearings is sufficient to overcome gravity.

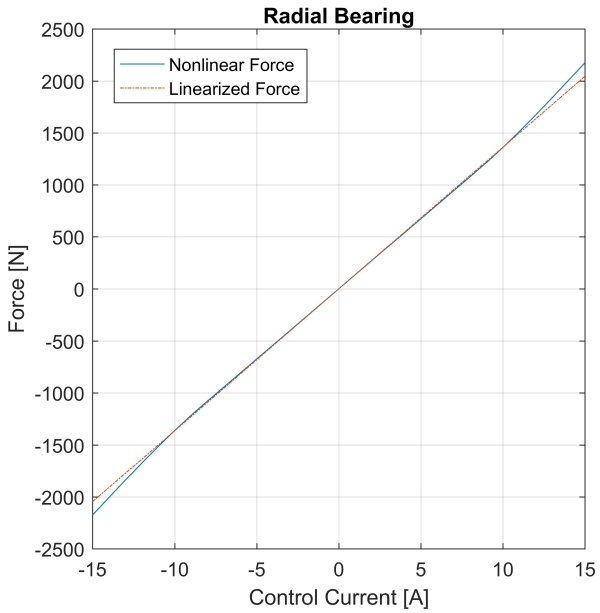

Fig. 4. Radial bearing nonlinear force for M19 steel when the rotor is in the center of the stator.

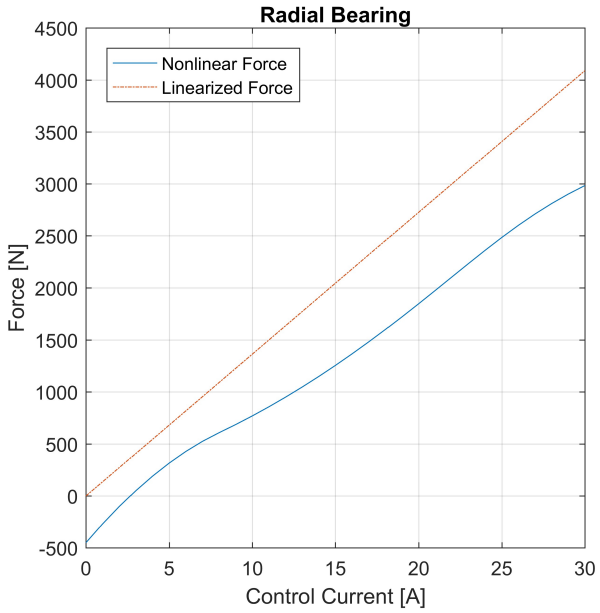

Fig. 5. Radial bearing nonlinear force for M19 steel when the rotor is at the limit of its motion.

V. AXIAL BEARING

The design process for the axial bearing is identical to the radial bearing design process except for some additional geometry and material constraints. The radial bearings utilize laminated stators and rotors to reduce eddy current loss, however the magnetic flux path of the axial bearings would require wedge shaped laminations to create the axial bearing annulus shape. Electrical steel is only available commercially in thin sheets so the axial bearing design is limited to less efficient magnetic materials. Since the axial bearing will be in direct contact with water, 410 grade martensitic stainless steel was chosen. For 410 grade stainless steel $B = 1\ T$ is the upper bound on the magnetic field strength to remain in the linear region of the B-H curve.

The axial bearing will have two concentric annulus surfaces on the stator for the magnetic flux to pass through to the rotor as shown in figure 6. The maximum magnetic flux is limited by the minimum cross sectional area of the axial bearing. This makes variations in the cross sectional area along the magnetic flux lines undesirable because they only add additional mass to the bearing. To optimize the mass of the axial bearing, the cross sectional area of the axial bearing annulus should be equal. In addition, we would like to separate the outer diameter of the smaller annulus and the inner diameter of the larger annulus by a gap larger than the thrust bearing airgap to reduce the magnetic forces between them and prevent a short circuit of the magnetic flux. Given the outer radius of the larger annulus r_o, the inner radius of the smaller annulus r_i, and the gap g_a we can calculate the smaller annulus outer radius r_i^m and the larger annulus inner radius $r_o^m = r_i^m + g_a$.

$$r_i^m = \frac{1}{2}\left(-1 + \sqrt{2r_i^2 + 2r_0^2 - 2g_a + 1}\right) \tag{12}$$

For the testbed the maximum force specification is three times the manufacturers expected force or 1800 N because of the higher uncertainty in the axial forces. Using (9) with a maximum magnetic field of 1 T the desired cross sectional area with is calculated as 2350 mm^2. The inner radius r_o is chosen as 43 mm to provide a large enough airgap between the axial bearing and shaft so that it is not creating significant radial forces. Using (12), the other axial bearing geometric parameters are $r_o^m = 34.2\ mm$, $r_i^m = 32.2\ mm$, and $r_i = 17\ mm$. The gap g_a is chosen to be 2 mm.

For a maximum magnetic field of 1 T and a maximum coil current of 20 A using (10) the

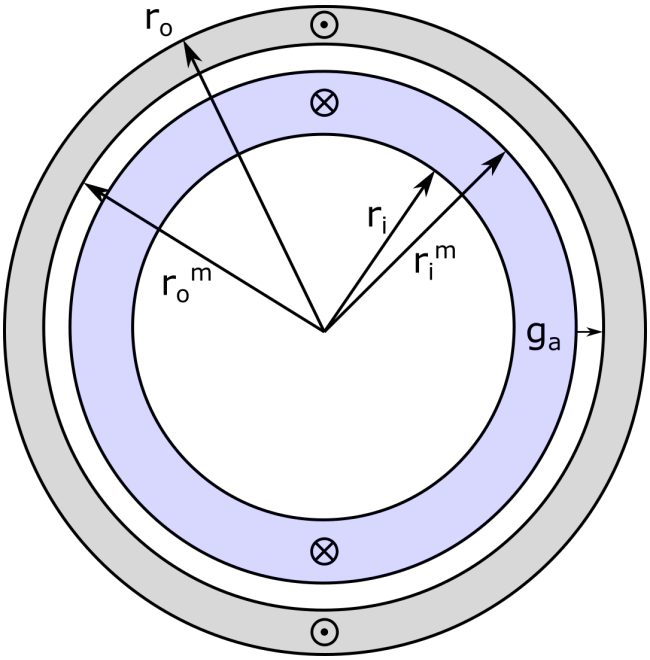

Fig. 6. Thrust bearing annuli and geometric quantities.

required number of turns for the axial bearing is 130. Like the radial bearing, 16 AWG wire was chosen for the axial bearing windings. With a cross sectional area of 1.3 mm^2 and a packing factor of 0.6, the minimum area for the coil is 518 mm^2.

With a bias current of 3.5 A and an airgap of 1.5 mm, the thrust bearing dynamics has the linearized coefficients

$$k_i = 465.4$$

$$k_x = 1085963$$

Figure 7 shows the nonlinear force when using 410 grade steel and the linearized force for the thrust bearing in bipolar mode. The maximum nonlinear force corresponds to the theoretical maximum force calculated in (9). Figure 8 shows the force response of the thrust bearing at the limit of the shaft travel. This figure shows that even at the limit of travel, the thrust bearing creates enough force to overcome the maximum expected axial force of 600 N.

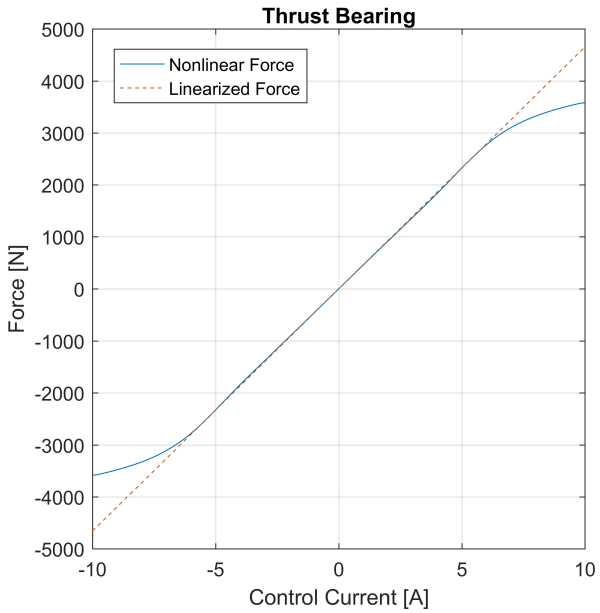

Fig. 7. Axial magnetic bearing force when centered.

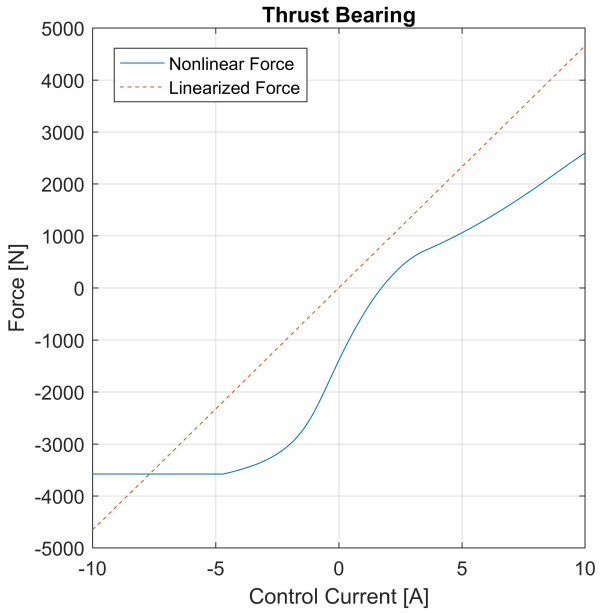

Fig. 8. Thrust bearing force at the limit of travel.

VI. COIL DYNAMICS

The geometry of the magnetic flux paths based on the force requirements of the testbed and the bias current define the dynamic behavior of the magnetic bearings. Developing an accurate model of the dynamics is the first step to designing a stabilizing controller. The dynamics of the magnetic bearing can be approximated by a linearized coupled model between the shaft motion and the coil current given by the differential equations

$$\ddot{x}(t) = \frac{k_i}{m} i(t) + \frac{k_x}{m} x(t) \tag{13}$$

$$\frac{di}{dt} = -\frac{R}{L} i(t) + \frac{1}{L} v(t) \tag{14}$$

where R is the coil resistance, L is the nominal coil inductance, $i(t)$ is the coil current, and $v(t)$ is the coil voltage. This model assumes that the coil inductance is constant given by the equation

$$L = \frac{\mu_0 A N^2}{2x_0} \tag{15}$$

There is a nonlinear dependence of the induction on the airgap size but the variations in the inductance are typically small. This nonlinear relationship is important to characterize for accurate application of an Extended Kalman Filter or Unscented Kalman Filter for state estimation and for some sensorless magnetic bearing control schemes that rely on the inductance variations to estimate the shaft position. Equation (15) also does not take into account manufacturing variability, eddy currents, magnetic field fringing, or magnetic field coupling. These unmodeled effects are difficult to accurately quantify theoretically or with numerical methods. To more precisely measure the dynamics of the coils, system identification experiments were performed on the testbed.

To capture the coil response over a wide range of frequencies, a chirp signal from 0.1 Hz to 400 Hz was chosen as the input voltage signal. The frequency response function from the input voltage to the coil current was calculated using

$$G(s) = \frac{Y(s)U(s)}{[U(s)]^2} \tag{16}$$

where $U(s)$ is the Fourier transform of the input voltage and $Y(s)$ is the Fourier transform of the measured coil current. The magnitude and phase of the frequency response function are shown in figure 9. The bandwidth of the open-loop coil response is approximately 55 Hz.

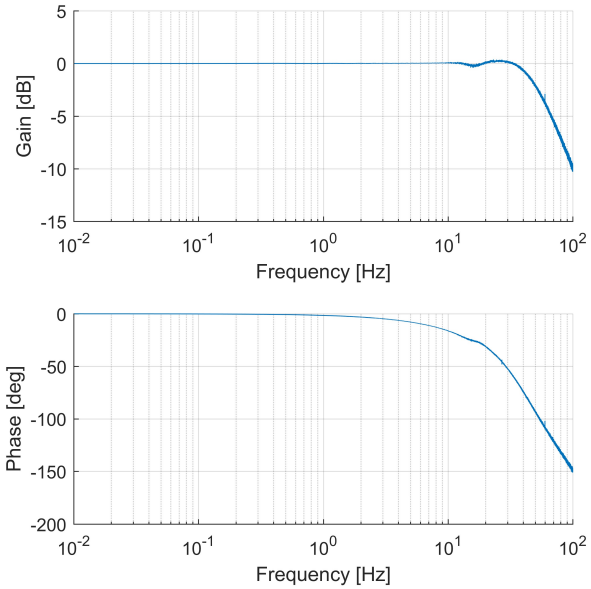

Fig. 9. Magnitude and phase of the radial bearing input/output relationship.

The experimental complex frequency response of the coil $G(s)$ was then used to identify the system transfer function model. Figure 10 validates the identified model by comparing the step response of the identified model to the step response of the coil current. While the designed number of turns for the radial bearing is 167 the actual number of turns in the assembled radial coils is 154; therefore for the radial magnetic bearing coils, the nominal theoretical inductance is 0.0128 H, the mean identified inductance is 0.0107 H, and the variance of the identified inductance is 1.83×10^{-7} H. The nominal theoretical inductance for the axial bearings is 0.0166 H while the identified model yields an inductance of 0.1722 H, which is an order of magnitude larger than expected.

The average identified coil resistance is 2.935 Ω which is slightly higher than the measured resistance at the output of the power electronics of 1.6 Ω.

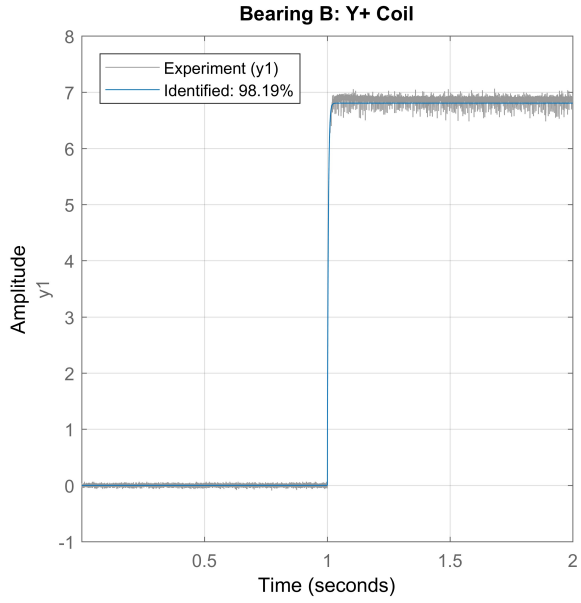

Fig. 10. Comparison of the step input response to the identified model response.

VII. CONCLUSIONS

In this paper the design of a fully submerged active magnetic bearing testbed was detailed with a focus on design procedures that do not ignore the complex interactions between the mechancial, electromagnetic, and control systems. Some initial experimental results identifying the dynamics of the magnetic bearing coils were also presented. The goal of this testbed is to mimic the dynamics of high-temperature molten salt pumps with canned rotors so that researchers can develop and test embedded I&C and state estimation for magnetic bearings in the presence of nonlinear hydrodynamic forces between the rotor and stator.

This testbed development is a step towards the development of high-temperature magnetic bearings that can operate in contact with high temperature fluids such as molten salts that are the primary coolant in molten salt reactors and large scale solar power generators.

Currently, the testbed assembly is complete and initial open-loop state-estimation experiments have been completed. To initially determine whether the linearized steady-state force model parameters are correct, the testbed shaft was manually positioned at different airgap values over the range of motion of the shaft and the coil control current was slowly increased until the bearing force was equal to the gravitational force on the shaft. While this test had high uncertainty

it provided confidence in the theoretical force model parameters.

The experimental data for the open-loop dynamic response of the coils showed a bandwidth of 55 Hz for the radial bearing and a bandwidth of 35 Hz for the axial bearing. This is below the 200 Hz bandwidth requirement due to the linearized spring constant or the 60 Hz bandwidth from the 3600 RPM operating speed of the pump. This lower bandwidth will make it difficult to find a stabilizing controller for the magnetic bearings. To increase the bandwidth of the coils, inner coil control loops with a proportional integral controller or a lead controller will be tested.

The experimentally obtained inductances for the radial magnetic bearings was within 16% of the nominal value. However, the measured inductance of the axial bearings is an order of magnitude larger than the theoretical value. This is likely due to the large eddy current losses because the axial bearing is not laminated. The experimentally obtained coil resistances are higher than the resistances measured at the output of the power electronics. This is due to the internal resistances of the power electronics.

The next steps in the research are the development of an initial stabilizing controller so that closed-loop system identification of the full system dynamics can take place. After model identification and validation, controllers will be designed using modern multi-variable control design techniques and tested to compare their performance. Finally, a signal modulation and a state-estimation based technique for estimating the shaft position based on the coupling between coil inductance and shaft position will be tested and compared.

ACKNOWLEDGMENTS

This material is based upon work supported by the U.S. Department of Energy, Office of Nuclear Energy, Nuclear Energy Enabling Technologies (NEET) program on Advanced Sensors and Instrumentation (ASI) under contract number DE-AC05-00OR22725.

REFERENCES

[1] R. A. Kisner, A. M. Melin, T. A. Burress, D. L. Fugate, D. E. Holcomb, J. B. Wilgen, J. M. Miller, D. F. Wilson, P. C. Silva, L. J. Whitlow, and F. J. Peretz, "Embedded Sensors and Controls to Improve Component Performance and Reliability: Conceptual Design Report," , Oak Ridge National Laboratory ORNL/TM-2012/433 (2012).

[2] A. M. Melin, R. Kisner, and D. L. Fugate, "Embedded Sensors and Controls to Improve Component Performance and Reliability: System Dynamics Modeling and Control System Design," ORNL/TM-2013/415, Oak Ridge National Laboratory (2013).

[3] A. M. Melin, R. A. Kisner, and D. L. Fugate, "Advanced Instrumentation and Controls for Extreme Environments," *IEEE Instrumentation and Measurement Magazine*, **16**, *3* (2013).

[4] S. K. Shaukat, J. E. Jackson, and D. F. Thatcher, "Regulatory Analysis for Generic Issue 23: Reactor Coolant Pump Seal Failure," NUREG-1401, IAEA (1991).

[5] J. E. Jackson, "Draft Regulatory Guide DG-1008 Reactor Coolant Pump Seals," DG-1008, NRC (1991).

[6] D. R. Diercks, "Analysis of Failed Nuclear Plant Components," *Materials Engineering and Performance*, **2**, *6*, 799 (1993).

[7] P. S. Pickard, "Sodium Reactor Experiment Accident July 1959," *Sandia National Laboratory* (2009).

[8] R. A. Kisner, D. L. Fugate, A. M. Melin, D. E. Holcomb, D. F. Wilson, P. C. Silva, and C. C. Molina, "Evaluation of Manufacturability of Embedded Sensors and Controls with Canned Rotor Pump System," , Oak Ridge National Laboratory ORNL/TM-2013/269 (2013).

[9] A. M. Melin, R. A. Kisner, D. L. Fugate, and D. E. Holcomb, "Hydrodynamic Effects on Modeling and Control of a High Temperature Active Magnetic Bearing Pump with a Canned Rotor," *NPIC&HMIT* (2015).

[10] A. M. Melin, R. A. Kisner, A. Drira, and F. K. Reed, "Embedded Sensors and Controls to Improve Component Performance and Reliability - Bench-scale Testbed Design Report," ORNL/TM-2015/584, Oak Ridge National Laboratory (2015).

[11] A. M. Melin and R. A. Kisner, "Embedded Sensors and Controls to Improve Component Performance and Reliability - Loop-scale Testbed Design Report," ORNL/TM-2016/563, Oak Ridge National Laboratory (2016).

[12] G. Schweitzer (Editor), *Practical Applications of the Active Magnetic Bearings to the Industrial World*, 225–244, Springer Berlin Heidelberg, Berlin, Heidelberg.

[13] A. Chiba, T. Fukao, O. Ichikawa, M. Oshima, M. Takemoto, and D. G. Dorrell, *Magnetic Bearings and Bearingless Drives*, Elsevier (2005).

[14] A. Traxler and E. Maslen, *Magnetic Bearings: Theory, Design, and Application to Rotating Machinery*, Springer (2010).

[15] H.-S. Dou, B. C. Khoo, and K. S. Yeo, "Instability of Taylor-Couette Flow between Concentric Rotating Cylinders," *Int. J. of Thermal Science*, **47**, *11*, 1422 (2008).

[16] J. Y. Hung, "Magnetic bearing control using fuzzy logic," *IEEE Trans. on Industry Applications*, **31**, *6*, 1492 (1995).

[17] P. V. S. Sobhan, G. V. N. Kumar, and J. Amarnath, "Rotor levitation by Active Magnetic Bearings using Fuzzy Logic Controller," *2010 International Conference on Industrial Electronics, Control and Robotics*, 197–201 (2010).

[18] H. S. Zad, T. I. Khan, and I. Lazoglu, "Design and Adaptive Sliding Mode Control of Hybrid Magnetic Bearings," *IEEE Transactions on Industrial Electronics*, **PP**, *99*, 1 (2017).

[19] Y. W. Tsai, V. D. Phan, and V. A. Duong, "Sliding mode control for active magnetic bearings of a flywheel energy storage system," *2016 IEEE International Conference on Control and Robotics Engineering (ICCRE)*, 1–5 (2016).

[20] G.-R. Duan and D. Howe, "Robust magnetic bearing control via eigenstructure assignment dynamical compensation," *IEEE Transactions on Control Systems Technology*, **11**, *2*, 204 (2003).

[21] M. Goto, T. Mizuno, I. Takami, and G. Chen, "Robust H-infinity control for Active Magnetic Bearing system with imbalance of the rotor," *2016 IEEE 14th International Workshop on Advanced Motion Control (AMC)*, 297–303 (2016).

[22] K.-Y. Lum, V. T. Coppola, and D. S. Bernstein, "Adaptive autocentering control for an active magnetic bearing supporting a rotor with unknown mass imbalance," *IEEE Transactions on Control Systems Technology*, **4**, *5*, 587 (1996).

[23] N. Morse, R. Smith, B. Paden, and J. Antaki, "Position sensed and self-sensing magnetic bearing configurations and associated robustness limitations," *Proceedings of the 37th IEEE Conference on Decision and Control*, vol. 3, 2599–2604 vol.3 (1998).

[24] J. Yu and C. Zhu, "Self-sensing active magnetic bearing using wavelet based position estimation algorithm," *2014 17th International Conference on Electrical Machines and Systems (ICEMS)*, 748–751 (2014).

[25] K. Matsuda, S. Kijimoto, and Y. Kanemitsu, "Self-Sensing Three-Pole Magnetic Bearing Using a Kalman Filter," *2006 SICE-ICASE International Joint Conference*, 1590–1594 (2006).

[26] K. K. MATSUDA and T. SAKAMOTO, "Unscented Kalman Filtering for Self-Sensing Magnetic Levitation against Magnetic Saturation," *Electrical Engineering in Japan*, **196**, *4*, 60 (2016).

[27] V. S. Lobanoff and R. R. Ross, *Centrifugal Pumps Design & Application*, Gulf Publishing Company (1985).